Controlled melting of a Wigner ion crystal with atomic resolution

Y.-Z. Xu,[1,*] W.-D. Zhao,[1,*] Y.-H. Hou,[1,*] Q.-X. Mei,[1] J.-Y. Ma,[1] J. Wang,[2,3] L. He,[1] Z.-C. Zhou,[1,4,†] Y.-K. Wu,[1,‡] and L.-M. Duan[1,§]

[1]*Center for Quantum Information, Institute for Interdisciplinary Information Sciences, Tsinghua University, Beijing 100084, People's Republic of China*

[2]*E. L. Ginzton Laboratory, Stanford University, Stanford, California 94305, USA*

[3]*Department of Applied Physics, Stanford University, Stanford, California 94305, USA*

[4]*Beijing Academy of Quantum Information Sciences, Beijing 100193, People's Republic of China*

(Received 17 August 2020; accepted 8 December 2020; published 28 December 2020)

The solid-liquid phase transition (melting) is a long-standing problem for which a complete understanding is challenging because of the strong many-body interactions. A trapped-ion Wigner crystal is a suitable platform for a controlled study of this phase transition with its unprecedented resolution of individual atomic ions. Here we study the melting dynamics of a linear chain of $^{174}Yb^{+}$ ions, which is initially cooled to the Doppler temperature and is then periodically heated and detected by a focused laser beam. We achieve controlled melting of the ion chain and observe unusual partial melting of long chains (coexistence of solid and liquid phases). We also observe a counterintuitive nonuniform energy distribution over the chain under localized heating. These results are further confirmed by molecular dynamics simulations to rule out other heating mechanisms.

DOI: 10.1103/PhysRevA.102.063121

I. INTRODUCTION

Phase transition is one of the central topics in physics. The solid-liquid phase transition, which has been known since ancient times, turns out to be a theoretical challenge despite lots of studies of its mechanism [1]. Ions in a Paul trap [2] or a Penning trap [3,4] provide an experimental platform for studying this melting phase transition with atomic resolution. At low temperatures, multiple trapped ions can form a solid phase under the long-range Coulomb interaction, which is known as a Wigner crystal [5,6]. Under different trapping potentials, one-dimensional (1D) [7], two-dimensional (2D) [8] or three-dimensional (3D) [9,10] ion crystals have been observed in experiments with a few to millions of ions.

At high temperatures, such ion crystals melt into a liquid phase (also known as an ion cloud in the literature) [11–14]. This phase transition (or a crossover for a finite system) has been observed in various experimental setups as the ions are heated by the electric field noise [15], the collision with the background atoms [16], and the interplay of the ions' chaotic motion and the oscillating rf fields in a Paul trap [13,17–20]. Incidentally, the melting of a Wigner crystal has also been studied in electronic systems, where individual electrons cannot be resolved but the phase-transition signal is extracted from the conductance of the material or the microwave resonance [6,21].

In the early days of ion trap research, strong heating effects existed and had to be balanced by a Doppler cooling laser beam; the study of the melting was thus based on the equilibrium properties at various temperatures by adjusting the parameters of the cooling laser [11]. With the improvement of the ion trap design, the intrinsic heating rate goes down and the lifetime of an ion crystal is significantly improved. This allows one to explore the dynamics under a controlled external heating mechanism; however, existing experiments are only in the low excitation regime below the melting point [22]. Besides, early studies of melting in the Paul trap mainly focused on the parameter regime near the Mathieu instability boundary [23,24]; results for small Mathieu parameters are lacking, which is preferable for recent experiments aimed at quantum computing as they provide stronger stability and smaller micromotion of the ions.

In this work, we study the controlled melting dynamics of a 1D chain of $^{174}Yb^{+}$ ions under typical experimental parameters for ion trap quantum computing experiments. Up to 22 ions are initially cooled to the Doppler temperature to form a linear chain, which is then periodically heated and detected until it melts. The controlled heating of the ions is achieved by a focused laser beam centered on a particular ion blue-detuned to the $^{2}S_{1/2}$-$^{2}P_{1/2}$ transition. The heating rate and location are tunable, which gives us a tool to study the nontrivial heat propagation inside the ion crystal during the heating process. This is also important for us to understand the destabilization and the heating mechanism of ion crystals under the collision of background gases, which is one of the major obstacles to realization of large ion crystals for quantum computing. Instead of direct observation of random collisions, here we realize a pointer heater on a particular ion in a controlled fashion. By analyzing the images of individual ions, we extract the phase transition signal and study the energy distribution over the ion chain during the heating process. Our work provides important tools to study the solid-liquid

*These authors contributed equally to this work.
†zichaozhou@mail.tsinghua.edu.cn
‡wyukai@mail.tsinghua.edu.cn
§lmduan@tsinghua.edu.cn

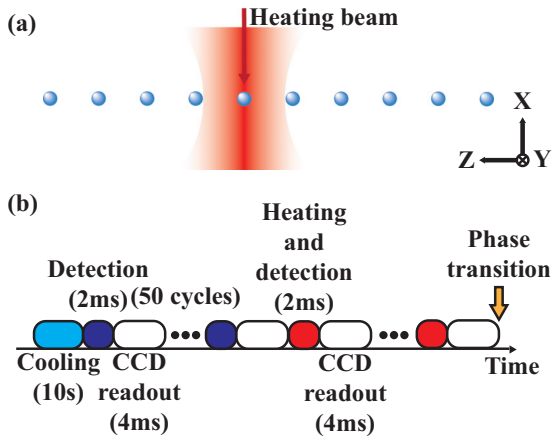

FIG. 1. (a) Schematic experimental setup. Ions are initially Doppler cooled by a global beam along the [1,0,1] direction (not shown in the figure) to form a linear chain along the z axis. A heating laser beam blue detuned to the $^2S_{1/2}$ - $^2P_{1/2}$ transition can be applied in the x direction to focus on any ion in the chain. By applying a resonant global detection beam (not shown) in the same direction as the cooling beam, the fluorescence of the ions can be collected by a CCD camera (not shown) in the y direction. (b) Schematic experimental sequence. The cooling, the detection, and the heating beams are only turned on in the indicated stages. The readout stage is for the CCD camera to process the signal with all these beams turned off. After the initial cooling stage, we repeat the detection-readout cycles 50 times to ensure that there is no visible intrinsic heating in the system. Then we turn on the heating beam while monitoring the signals on the CCD camera until the ion chain melts.

phase transition and can also be important for the stabilization of large crystals for their various applications [25,26] such as quantum information processing [27] and precision measurement [28].

II. CONTROLLED MELTING OF AN ION CHAIN

Our experimental setup is shown schematically in Fig. 1(a). $^{174}Yb^+$ ions are trapped in a four-rod trap with trap frequencies $\omega_r \approx 2\pi \times 1.572$ MHz and $\omega_z = 2\pi \times 114$ kHz, which corresponds to a Mathieu parameter $q \approx 0.3$. The principal axes of the trap in the radial directions are at 45° to the x and the y axes. The ions are initially cooled close to the Doppler temperature on the order of 1 mK by a global 369-nm laser beam which is 10 MHz red detuned to the $^2S_{1/2}$ - $^2P_{1/2}$ transition. The cooling beam is along the [1,0,1] direction with nonzero projections on all the three principal axes of the trap and hence can cool the motion of the ions in all spatial directions. We also estimate the temperature as $T = 7$ mK by a Gaussian fitting to the ion's profile in the CCD images [29]. After forming a linear chain of 10 to 22 ions with a separation of about 5–10 μm, individual ions can be selectively heated by a controllable heating beam which is 20 MHz blue detuned to the $^2S_{1/2}$ - $^2P_{1/2}$ transition [30]. The power of the heating laser is about 550 μW. Its intensity has a Gaussian profile $I(r) \sim \exp(-\frac{r^2}{2\sigma^2})$ which is shown as the red laser beam in Fig. 1(a), with a width of about $D \equiv 2\sqrt{2}\sigma = 8.5$ μm. This beam width leads to small laser intensity on adjacent ions when the heating beam is centered on one ion, but the heating effect is still local and thus allows us to study the energy distribution over the chain under the controllable local heating. Later in numerical simulations, we still selectively heat one ion for simplicity and expect the qualitative behavior to be the same as in the experiment. We also change the position of the heating beam on different ions to study how it affects the melting of the ion chain.

The experimental sequence is presented in Fig. 1(b). After the ions are loaded and cooled into a linear chain, first we image the ions for 50 detection cycles without the heating beam to ensure that intrinsic heating in the system has negligible effects on the melting. Then we switch on the controllable heating beam while monitoring the image of the ions until the ion chain melts.

In Fig. 2 we achieve the controlled melting of a chain of 10 ions. In the beginning, the image of each ion (see Appendix B) is a small bright spot and shows no significant change during the 50 detection-readout cycles, which suggests that the ions are localized and thus the system stays in the ion crystal phase at low temperature. Then we turn on the heating beam on an arbitrarily chosen ion. As the kinetic energy of the ions increases, so do their amplitudes and therefore the sizes of the bright spots in the image. In the meanwhile, the brightness of each spot is decreased, not only because the photon counts are distributed in a wider range, but also due to an increased Doppler shift of the detection beam from the increased velocity of the ions and hence the reduced scattering rate of photons. After a few heating-and-detection-readout cycles, the images of the ions suddenly disappear on the CCD camera, which indicates a transition to the ion cloud phase. This is probably because the ions now obtain enough energy to go across the energy barrier in the potential; therefore, the ions exchange positions much more frequently after the melting point and can move in a much wider range in space. Quantitatively, we can plot the average photon counts of the ion chain and use the fastest rate of change as the indicator of the melting point, as shown in Fig. 2(a). We also vary the position of the heating beam along the ion chain and find that it has no significant influence on the melting dynamics (the data are similar and are not shown here).

To further confirm the observation of the controlled melting and to rule out the possibility that the transition is caused by heating mechanisms other than the blue-detuned laser beam, we also perform molecular dynamics simulation using the same trapping and laser parameters as the experiment. Here we model the oscillating trapping potential by a harmonic pseudopotential [30] and use a fourth-order symplectic integrator [31] to solve the equation of motion of the ions. To suppress the discretization error, we choose a step size between 0.5% and 4% of the transverse trapping period $2\pi/\omega_r$. The force due to the heating beam is modeled by the velocity-dependent scattering of the photons [12]. Here we have a heating laser beam with a wave vector $\vec{k}$ along the x direction, a detuning $\Delta = 2\pi \times 20$ MHz to the $^2S_{1/2}$ - $^2P_{1/2}$ transition and a saturation parameter $s = 2|\Omega|^2/\Gamma^2$ [30]. When an ion has a velocity $\vec{v}$, the velocity-dependent detuning of the heating laser beam becomes $\Delta_{\text{eff}} = \Delta - \vec{k} \cdot \vec{v}$. For the spontaneous emission rate of $\Gamma = 2\pi \times 20$ MHz of the $^2P_{1/2}$ level, the scattering rate is $\Gamma\rho_{ee}$ where $\rho_{ee} = (s/2)/[1 + s +$

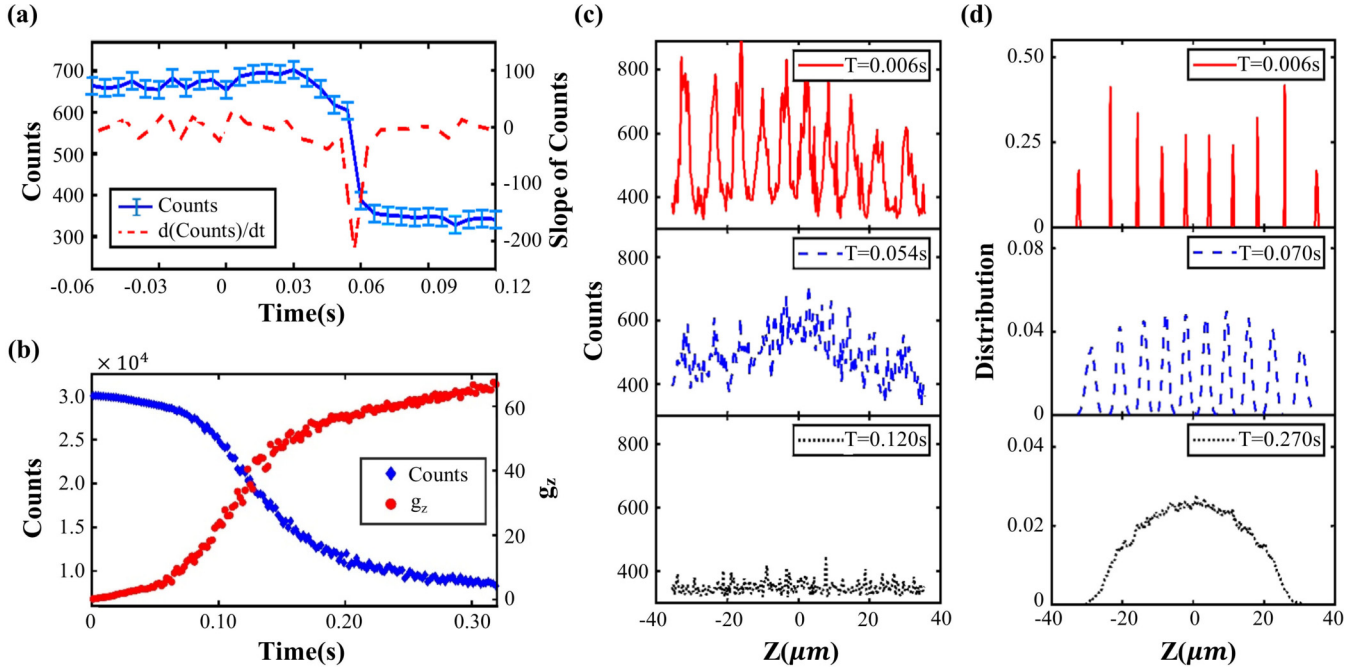

FIG. 2. Controlled melting of an ion chain. (a) The blue curve is the average photon counts of the ion chain $\sum_i C_i/N$ (with error bars estimated from the dark count of the CCD camera) versus time, where C_i is the average photon count in a box surrounding the ith ion (see Appendix B for the raw image and more details) and N is the total number of ions. The heating laser is applied at $t = 0$ s. The red dashed curve is the rate of change of the photon counts. The fastest rate of change at $t = 0.054$ s indicates the melting point. (b) Theoretical results for a numerical simulation with ten ions under similar experimental parameters. The blue diamond and the red circle data points are the number of scattered photons and the diffusion parameter g_z, respectively. A sharp change of the behavior can be observed around $t = 0.07$ s, which indicates a phase transition. (c) The count distribution of the ten ions along the axial z axis at time $t = 0.006$ s (the crystal phase, red solid), $t = 0.054$ s (the melting point, blue dashed), and $t = 0.120$ s (the ion cloud phase, black dotted). Each data point is averaged over the transverse x direction. We plot the three curves using the same scale to show the overall decay in the photon counts. These curves reflect the spatial structure of the system in different phases. (d) The probability distribution of the ten ions along the z axis in the same numerical simulation as (b) at time $t = 0.006$ s (the crystal phase, red solid), $t = 0.070$ s (the melting point, blue dashed), and $t = 0.27$ s (the ion cloud phase, black dotted). Each curve is computed from the positions of the ions in a time interval of $\Delta T = 0.002$ s.

$(2\Delta_{\text{eff}}/\Gamma)^2]$ is the population of the $^2P_{1/2}$ level. Each scattering event includes the absorption of a photon in the direction of the heating beam together with the emission of a photon in a random direction, and it occurs at the probability of $\Gamma\rho_{ee}\Delta T$ for a small time interval ΔT.

We use two observables in the numerical simulation to study the melting of the ion chain. The first one is the number of scattered photons from all the ions during a short time interval ΔT, which we choose to be the same as the experimental exposure time of 0.002 s. This observable is proportional to the photon counts collected by the CCD camera in the experiment. The second observable is the axial diffusion coefficient $g_z = \sum_{i=1}^{N} \Delta z_i^2/N\Delta T$, where Δz_i is the displacement of the ith ion along the z direction in the time interval ΔT [13]. More details can be found in Appendix C. In Fig. 2(b), we plot the simulated average photon counts and g_z per ion as the blue and the red dots. A relatively sharp change of the behavior, in particular for g_z, can be observed around $t = 0.07$ s, which is on the same order of magnitude as the melting time of $t = 0.054$ s observed in the experiment.

To further demonstrate the change in the structure of the ion crystal during the melting process, we plot the experimental count distribution along the axial z direction in Fig. 2(c). In the crystal phase ($t = 0.006$ s), the count distribution shows well-separated peaks corresponding to each of the ions. Near the transition point ($t = 0.054$ s), the peaks become wider and start to merge together. Finally in the ion cloud phase ($t = 0.120$ s) the distribution further flattens out and it becomes difficult to resolve peaks for individual ions (note that here we do not show the error bars on the order of tens of counts for clarity).

Similarly, in Fig. 2(d), we plot the numerically simulated distribution of the ions along the z axis in a short time period ΔT before (red), after (black), and right at the melting point (blue). The qualitative behavior for the experimental and the numerical results agrees well in all these three stages, although the exact time points for the melting to occur differ. This difference may come from our simplified theoretical model in the numerical simulation. As mentioned above, we ignore the micromotion of the ions and model the trapping potential by a harmonic trap; we also neglect the small laser intensity of the heating beam on the adjacent ions. Besides, when we repeat the experiment under the same set of parameters, the melting time also varies due to the fluctuation in some parameters. Nevertheless, since the phase-transition dynamics in the experiment and in the simulation still occur on the same time scale, we believe that our numerical simulation already successfully characterizes the dominant melting mechanism.

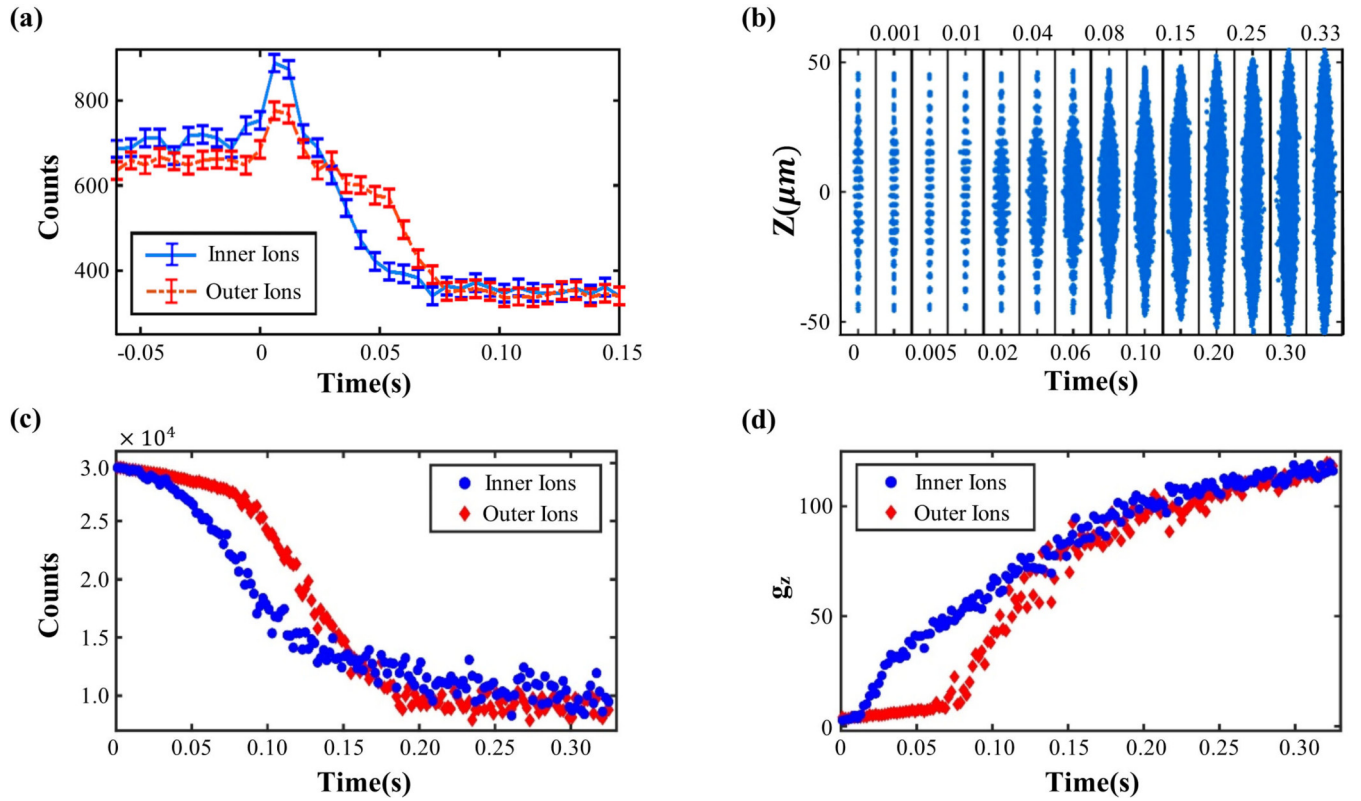

FIG. 3. Partial melting from the center of an ion chain. (a) Average photon counts of the three innermost ions (blue solid) and the three outermost ions on each end (red dashed) versus time (see Appendix D for the raw image). The photon count for the inner ions goes down earlier than that for the outer ions, which suggests that the melting occurs from the center to the edges. The error bars are estimated from the dark count of the CCD camera. (b) Simulated distribution of ions in the x-z plane during a short time interval $\Delta T = 0.002$ s starting from various time points (labeled on the top and the bottom) assembled from left to right. The plotted region is between $x = \pm 3$ μm and $z = \pm 52$ μm. (c) Simulated average photon counts for the inner (blue circles) and the outer (red diamonds) ions under the similar experimental parameters with an ion in the center being heated. The average count for the inner ions drops faster than that for the outer ions and the tendency agrees well with the experimental result. (d) The diffusion parameter g_z for the inner (blue circles) and the outer (red diamonds) ions from the same simulation. This observable shows sharper changes than the photon counts and we can read the melting point for the inner ions to be $t = 0.02$ s, which is earlier than that for the outer ions near $t = 0.07$ s.

III. PARTIAL MELTING FROM THE CENTER

Apart from the above global melting phenomenon, we also observe unusual partial melting by varying the trapping parameters or the number of ions. In Fig. 3 we keep the same trapping potential but increase the number of ions to 22 (see Appendix D for the raw image, with 17 bright ions and 5 dark ions which may be caused by the reaction with a background hydrogen molecule into an YbH^+ or a leakage into the $^2F_{7/2}$ level). In this case, apart from the ion crystal and the ion cloud phases, we also observe an intermediate partial melting phase where the central ions already melt but those on the edges still maintain the crystal structure. This partial melting phenomenon has also been predicted in 3D ion crystals through numerical simulations [32,33].

Quantitatively, we plot the average photon count from the innermost three ions (inner ions) and that from the outermost three ions on each side (outer ions) in Fig. 3(a). The photon count for the inner ions drops faster than that for the outer ions in the intermediate region with a separation larger than the error bars. Note that, although five dark ions exist in this example, possibly due to the formation of YbH^+ ions, this does not change the qualitative behavior of melting because the relative change in the mass of the ion is small and we only need some of the bright ions to feel the heating laser beam to drive the melting phase transition.

Again, we further support our experimental observations by numerical molecular dynamics simulations under similar parameters. In Figs. 3(c) and 3(d), we plot the counts and axial diffusion parameters for the inner ions and the outer ions as defined above. Similar to Fig. 2(b), the average photon count generally decreases and the diffusion parameter increases as the ion crystal heats up and melts. However, for the inner ions, both these phenomena occur earlier than those for the outer ions, which indicates a partial melting of the ion chain from the center. The tendency in the simulated photon counts agrees well with the experiment and again their time scales are on the same order of magnitude. Furthermore, the simulated diffusion parameter shows a sharper change than the photon counts and indicates a melting time of $t = 0.02$ s for the inner ions and $t = 0.07$ s for the outer ions. In Fig. 3(b) we simulate the distribution of the ions on the x-z plane for a better illustration of their spatial structure. We observe that the distribution of the inner ions merges first in the partial

melting stage between $t = 0.02$ s and $t = 0.07$ s, while that for the outer ions is still distinct. A similar phenomenon is also observed in the experimental images shown in Appendix D.

Similar to the global melting, this partial melting phenomenon is not sensitive to the location of the heating beam as we vary it in the experiment or in the numerical simulation. Also we observe that under the same trapping parameters, partial melting tends to occur more easily for higher ion numbers.

IV. NONUNIFORM ENERGY DISTRIBUTION AND REFLECTION SYMMETRY

As evident from Fig. 3, the energy distribution over the ion chain during the melting process is not uniform and shows a reflection symmetry when the heating beam is applied at the center of the chain. This reflection symmetry has been predicted in theory in Ref. [34] for a weak driving.

Here we confirm this statement in the experiment in Fig. 4. In Fig. 4(a), we consider a chain of ten ions (eight bright ones and two dark ones) heated at the two central ions. We select two time slices during the evolution, one in the ion crystal phase and the other in the intermediate partial melting phase, and plot the distribution of photon counts of each ion. In the partial melting case, the central ions cannot be distinguished, so the photon counts are collected in manually assigned boxes as shown in Appendix B and Appendix D. In both cases, we observe nonuniform distribution and a rough reflection symmetry in the photon counts within the estimated error bars. Note that, in the crystal phase, the three central ions are much brighter than the others. This is due to the existence of the focused heating laser beam which generates more scattered photons from the ions on which it is shined, even though it is blue detuned from the atomic transition. Furthermore, here the error bars only reflect the influence of the dark counts of the CCD, while there can also be small systematic spatial variation in photon counts due to the nonuniform intensity distribution of the global detection beam and imperfection in the imaging system.

In the experiment, we need the heating beam to be at the center of the ion crystal to preserve the reflection symmetry because the heating beam itself can cause the additional scattering of photons. On the other hand, in numerical simulation we can directly look into the motion of the ions through simulated photon counts and the axial diffusion parameter g_z. As we show in Figs. 4(b)–4(d), even if the heating beam is applied on the edge of the ion chain, the response of the ions still shows reflection symmetry. This is because the eigenmodes of the linear chain have the reflection symmetry; since the heating beam is weak, the system approximately establishes equilibrium at each time and thus follows the symmetry of the eigenmodes [34]. As we verify in the numerical simulation, when heated at different positions of the ion chain, the reflection symmetry stays unchanged.

V. DISCUSSION AND CONCLUSION

Melting of an ion crystal is a complicated physical process which involves chaotic dynamics of multiple ions [17]. In this experiment and the corresponding numerical simulation,

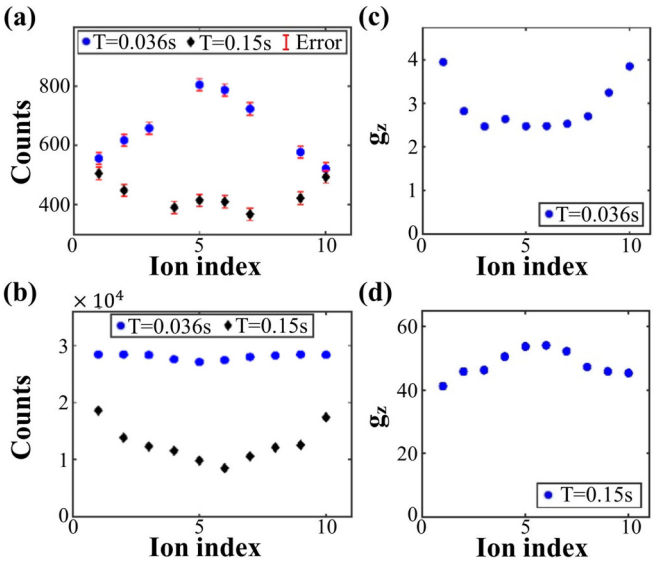

FIG. 4. Nonuniform energy distribution and reflection symmetry. (a) Photon count distribution C_i of a chain of ten ions heated on the two central ions at time $t = 0.036$ s (ion crystal, the sixth detection cycle since heating, represented by blue circles) and $t = 0.15$ s (partial melting, the 25th detection cycle since heating, represented by black diamonds). The positions for the dark ions are left empty. Between these two time points, one dark ion (the fourth ion on the left) has exchanged positions with a nearby bright ion (the third on the left). Here, the error bars are estimated from the dark counts of the CCD camera. In the partially melted case, the central ion spots cannot be distinguished; hence the corresponding C_i's are counted in manually assigned boxes (see Appendixes B and D for details together with the raw image). (b) Simulated counts for each of the ten ions under the same trapping potential at $t = 0.036$ s (ion crystal, represented by blue circles) and $t = 0.15$ s (ion cloud, represented by black diamonds). The heating beam is turned on at $t = 0$ on the first ion on the left. The data are computed for a short time interval $\Delta T = 0.002$ s. (c), (d) Axial diffusion parameter g_z for each of the ten ions from the same numerical simulation as in (b) at (c) $t = 0.036$ s and (d) $t = 0.15$ s. The data of g_z are computed for a time interval $\Delta T = 0.002$ s. Before and after the melting point, the values of g_z change significantly so they are not plotted in the same scale.

we observe clear evidence of controlled melting of a 1D ion crystal using two order parameters, the average photon counts and the axial diffusion parameter. The study of the melting dynamics of an ion chain plays a crucial role in its application in quantum information processing tasks. It has been known that the lifetime of long ion chains decreases with the number of ions [35]. Therefore, the stabilization of ion crystals becomes increasingly important as the number of ionic qubits rises. Our results about the melting dynamics already provides important hints about how an ion crystal can be stabilized. For example, by monitoring the images of ions on the edges, we may determine when the ion chain starts to melt or prevent it from happening by applying a cooling beam so as to prolong the lifetime of long ion chains. Besides, since the ions on the edges generally have higher kinetic energy in the initial stage of the melting [see, e.g., Figs. 4(a) and 4(c)], the system may be effectively cooled if we selectively apply the cooling beams on these two ions.

To sum up, we realize controlled melting of a linear chain of ions and study its dynamics in the experiment with atomic resolution. Phenomena such as partial melting from the center of the chain, nonuniform energy distribution, and its reflection symmetry are observed. This work deepens the understanding of the solid-liquid phase transition of ion crystals and provides important hints about stabilizing large ion crystals and increasing their lifetime in the future.

ACKNOWLEDGMENTS

This work was supported by the Beijing Academy of Quantum Information Sciences, the National Key Research and Development Program of China (Grant No. 2016YFA0301902), Frontier Science Center for Quantum Information of the Ministry of Education of China, and Tsinghua University Initiative Scientific Research Program. Y.-K.W. acknowledges support from the Shuimu Tsinghua Scholar Program and International Postdoctoral Exchange Fellowship Program (Talent-Introduction Program).

APPENDIX A: EXPERIMENTAL DETAILS

The experiments are performed in a four-rod ion trap with a spherical octagon vacuum chamber (see Fig. 5). The radio-frequency (rf) voltage is applied on a pair of electrodes and the dc voltage is applied on the end caps to generate a quadrupole potential which is used to confine the $^{174}Yb^{+}$ ions. The rf signal is generated with a signal generator at 15.3 MHz, and is then amplified by a commercial power amplifier. The amplitude of the rf voltage is controlled by a voltage variable attenuator (VVA), ranging from 200 to 500 V. The end-cap electrodes can be applied with ± 20 V dc voltages, which are used to adjust the confinement potential and the micromotion. The potential depth is about 5–10 eV in our experiment.

370-nm lasers modulated with acousto-optic modulators (AOMs) are used for most operations on the ions including cooling, heating, and detection. The relative detuning of the beams are the protection beam (without modulation), the cooling beam (+240 MHz sideband), the detection beam (+250 MHz), and the heating beam (+270 MHz). These AOMs are driven by amplified rf signals from direct digital synthesis (DDS) circuits. A field-programmable gate array (FPGA) is used to control each of these signals, so that we can switch these beams in microseconds. In addition, the frequency of the laser is actively stabilized by a cathode lamp system with a digital proportional-integral-derivative (PID) lock such that the detection beam is resonant with the atomic transition. The ^{174}Yb atoms are generated by pulse laser ablation [36,37], excited to the $^{1}P_1$ level by a 399-nm laser beam and are then ionized and Doppler cooled by the protection beam. Then, these ions are further cooled into a Wigner crystal with the cooling beam. The fluorescence of the ions is collected by an object with NA $= 0.33$ and is imaged with an electron-multiplying charge coupled device (EM-CCD). We also use a 935-nm laser beam to repump the ions in the $^{2}D_{3/2}$ state back to the ground state.

The data collection of the EM-CCD is controlled by an FPGA. In each cycle, the EM-CCD is first exposed for 0.002 s (the shortest time to distinguish the signal from the background noise) and then the data are read out for 0.004 s (limited by the data transfer rate of the CCD).

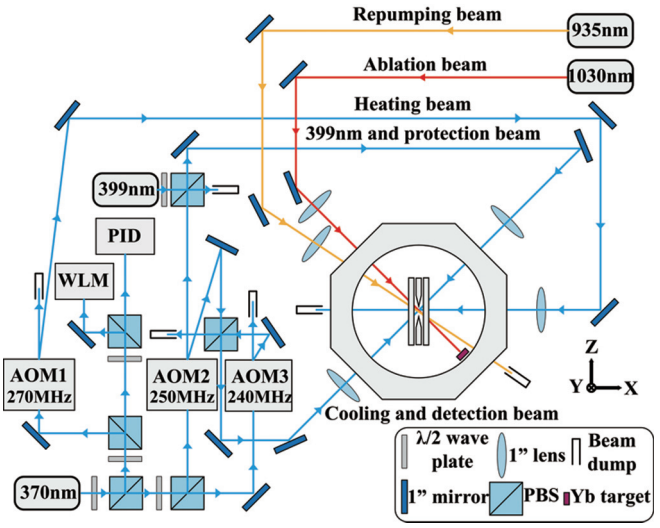

FIG. 5. Schematic of the experimental system. The PID represents the whole frequency stabilization system that detects the frequency fluctuation of the 370-nm laser and feeds back to the diode laser with a digital PID lock. The WLM represents a wavelength meter. Ions are initially Doppler cooled by a global cooling beam to form a linear chain along the z axis. A heating laser beam can be applied in the x direction to focus on any ion in the chain. By applying a resonant global detection beam, the fluorescence of the ions can be collected by a CCD camera in the y direction. 1030- and 935-nm laser beams are used for laser ablation and repumping, respectively, which enter from the same view port on the left of chamber.

APPENDIX B: ION IMAGE RECOGNITION AND DATA PROCESSING

The experimental data are the images from the EM-CCD (with settings exposure time, 0.002 s; gain factor, 1000; with electron multiplication, refresh rate, 17 MHz). Each image has a size of 512×35 pixels. The amplification ratio of our imaging system is $35.5\times$. The actual dimension of a single pixel is about 0.45 μm.

As shown in Fig. 6, we divide the image of ions into boxes to extract the photon counts for each ion, C_i. This division can be achieved by the following image-processing algorithm.

First we perform noise reduction and image binarization followed by another noise reduction. Then, the bright spots and the dark background can be distinguished by a predetermined threshold. Finally, the ion boxes can be extracted according to the 8(6)-connectivity connected-component labeling algorithm [38]. Two examples are shown as the red boxes in Fig. 6(a). However, the probability of a successful recognition decreases rapidly when the ion chain melts because the fluorescence becomes too low. In such cases, the boxes can also be assigned manually to help the algorithm to recognize the positions of the ions.

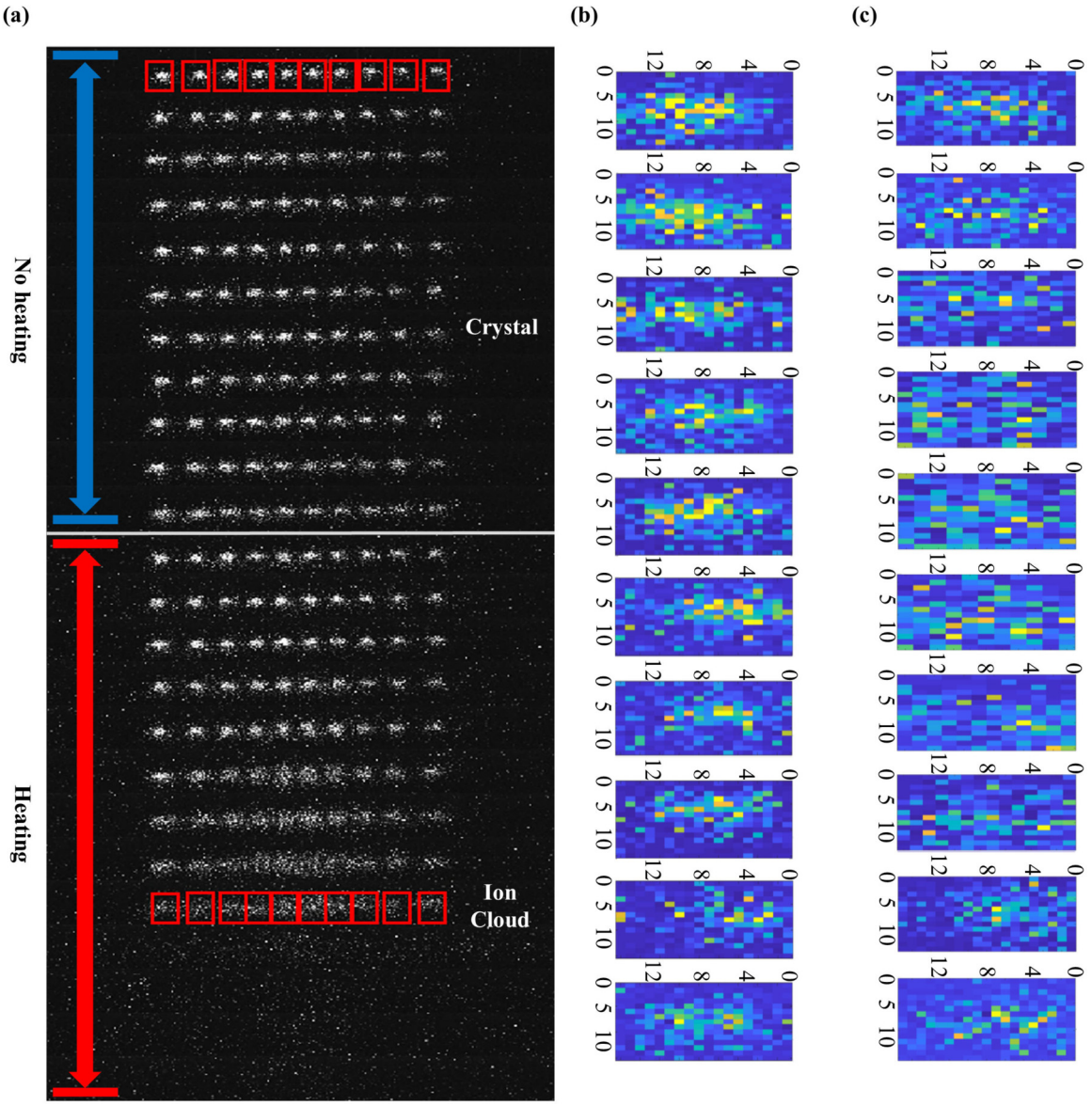

FIG. 6. The experimental images for the data in Fig. 2(a) of the main text. (a) A chronological combination of images of a chain of ten ions assembled from top to bottom. Each row corresponds to the image during one detection stage. The white horizontal line separates the detection-readout cycles and the detection-and-heating-readout cycles in Fig. 1(b) of the main text. Above this line without the heating beam, the structure of the ion chain shows no significant changes during the 50 cycles (only the last 11 cycles are shown here for simplicity). Below this line with the heating beam on, the amplitudes of the ions increase, the images blur, and finally the ion chain melts after nine cycles with the individual ions no longer visible. Here the controllable heating beam is focused on the third ion on the left. Examples of red boxes surrounding individual ions are presented in two rows with sizes of 15×12 pixels (which is $6.75 \times 5.4\ \mu\text{m}^2$ in actual dimension) to extract the photon counts C_i for each ion. See Appendix B for details about the choice of boxes. (b) The images of the ten ion boxes in the first row of (a). Before melting, ions can be easily recognized as the bright spots at the center of each box. (c) The images of the ten ion boxes in the last row of (a) before melting.

APPENDIX C: OBSERVABLES FOR NUMERICAL SIMULATION

In this work, two observables, the axial diffusion parameter g_z and the number of scattered photons, are used to study the melting in the molecular dynamics simulation.

The general diffusion parameter g_θ is defined as

$$g_\theta = \frac{\sum_{i=1}^{N} d_{i,\theta}^2}{N\Delta t}, \tag{C1}$$

where $d_{i,\theta}$ is the displacement of the ith ion projected to the direction θ ($\theta = x$, y, z or other directions) in the time interval Δt, and N is the total number of ions. For the melting of a 1D ion chain, we use g_z as the observable because the motion in the axial direction is more significant than those in the transverse directions. When studying the partial melting and the energy distribution, we have also used the diffusion parameter for a subgroup of ions or even the individual ions. This generalization is straightforward where we simply per-

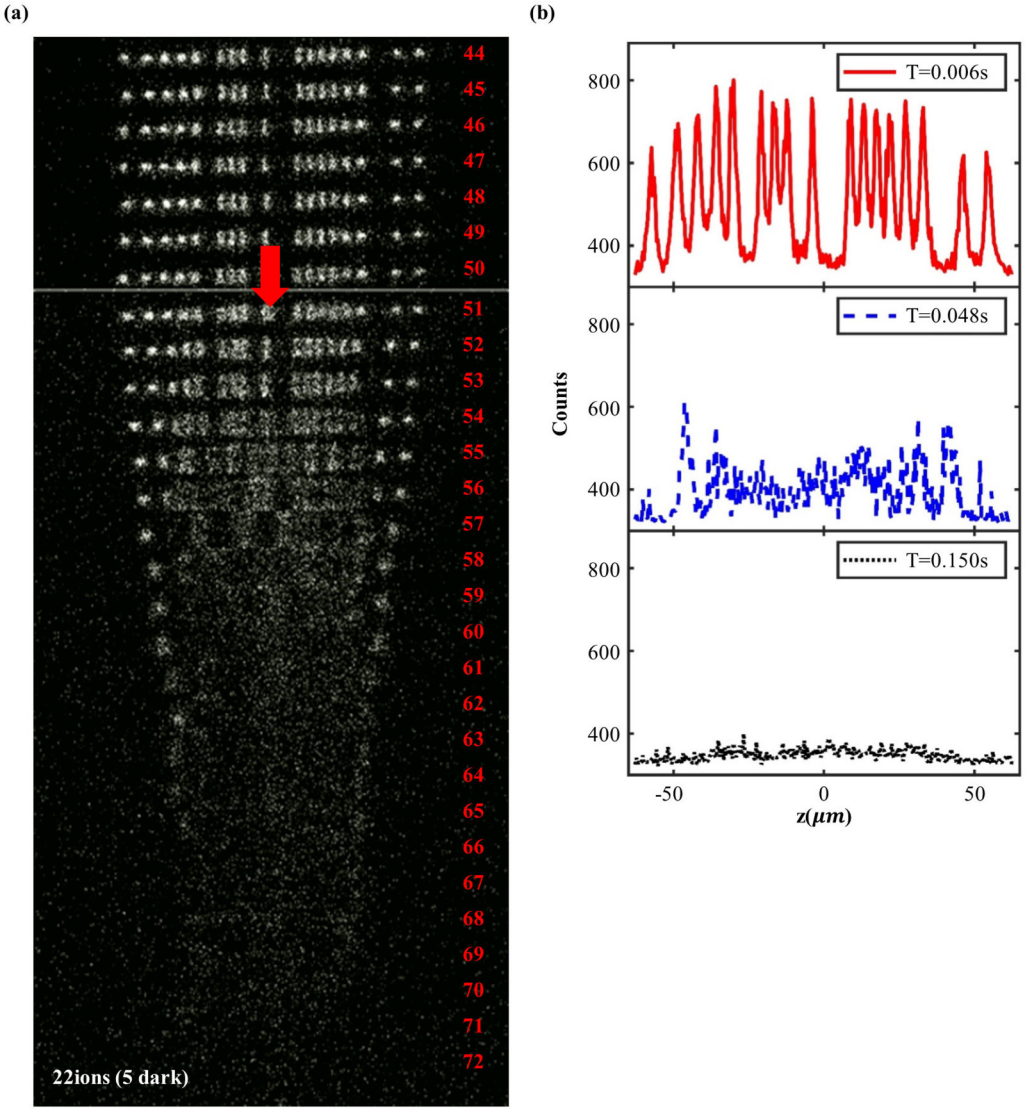

FIG. 7. (a) The experimental images for the data in Fig. 3(a) of the main text. It is a chronological combination of images of a chain of 22 ions (17 bright ions and 5 dark ions) assembled from top to bottom. Each row corresponds to the image during one detection stage. The white horizontal line separates the detection-readout cycles and the detection-and-heating-readout cycles. After the heating beam is applied on the two central ions, the spots of the ions get dimmer, which indicates an increased temperature with time. However, the sizes of the spots for inner ions are clearly much larger than those for the outer ions on the edges. After about six heating-and-detection-readout cycles, the inner ions already seem to melt as their spots merge together, while the spots of the two ions on the edges are still sharply distinct. Then after another four cycles the spots of the outer ions also join the central cloud and the ion crystal completely melts. Also note that during this process the overall size of the system is shrinking in the z direction. This is likely because the central ions get larger amplitudes in the x and the y directions and thus the outer ions feel a reduced Coulomb repulsion along the z axis. (b) The count distribution of the 22 ions along the axial z axis at time $t = 0.006$ s [ion crystal, red solid line, the first detection cycle since heating, labeled as 51 on the right of (a)], $t = 0.048$ s (partial melting, blue dashed line, the eighth detection since heating), and $t = 0.150$ s (ion cloud, black dotted line, the 25th detection cycle since heating). Each data point is averaged over the transverse x direction. The red line shows well-separated peaks indicating a crystal structure. In the partial melting case (blue dashed line), the count distribution of the outermost ions still shows well-separated peaks, but those for the inner ions start to be indistinguishable from the experimental noise. Finally in the ion cloud phase (black dotted line), the photon count further decays and the distribution becomes much smoother, which indicates that the crystal has melted.

form the summation over the subgroup and replace N by the number of ions in it.

The scattered photon counts from the ith ion can be computed from its scattering rate $dN_i/dt = \Gamma\rho_{ee}(\vec{v}_i)$ as defined in the main text, where we assume a global detection beam in the direction of $[1, 0, 1]$. In the experiment, we define boxes to extract counts of individual ions. For the convenience of comparing with the experiment, we also define a box in the numerical simulation. In the simulation, the position, the velocity, and the corresponding scattering rate of photons are known for each ion at each time point. We can thus attribute the photon counts $dN_i(t)$ from the ith ion in a short time

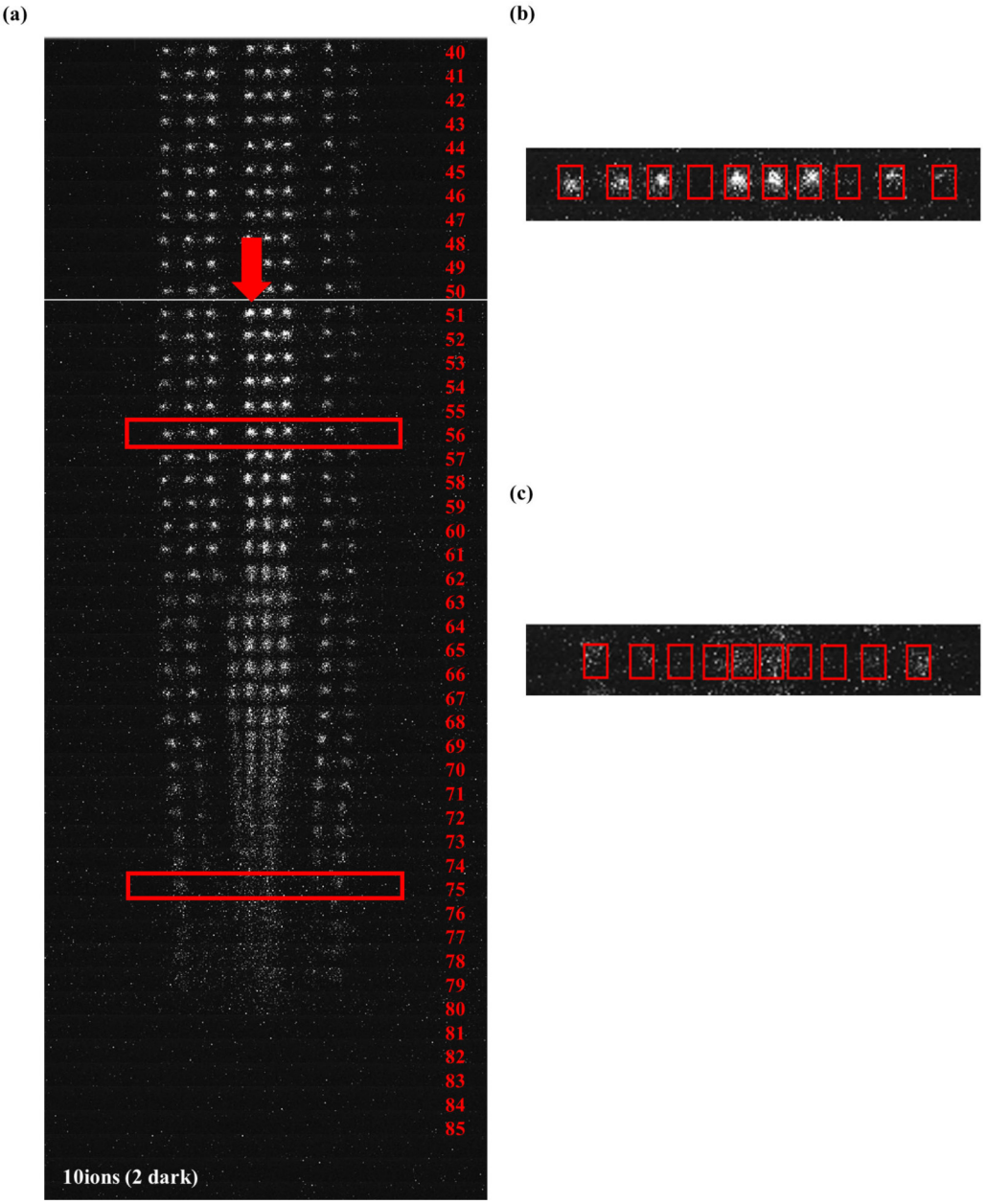

FIG. 8. (a) The experimental images for the data in Fig. 4(a) of the main text. (b) The time slice for the data at $t = 0.036$ s [the sixth row after heating in (a)] with the boxes to count the photons from each ion presented. The system is in the crystal phase. (c) The time slice for the data at $t = 0.15$ s [the 25th row after heating in (a)] with the boxes to count the photons from each ion presented. The ion chain is partially melted.

interval $[t,\ t + dt]$ to the spatial location $(x(i,t), z(i,t))$ of the ion.

Then we can define the box for each ion with a similar size as those used in the experiment to calculate the simulated counts. First, the center of a box is located at the average position of the corresponding ion duration the time interval ΔT, which we label as $(X_{\rm box}(i,t), Z_{\rm box}(i,t))$:

$$X_{\rm box}(i,T) = \int_{T}^{T+\Delta T} \frac{x(i,t)}{\Delta T} dt, \tag{C2}$$

$$Z_{\rm box}(i,T) = \int_{T}^{T+\Delta T} \frac{z(i,t)}{\Delta T} dt. \tag{C3}$$

The range of the ith ion's box at time $t = T$ is

$$\begin{aligned}\text{Range}(i,T) = &[X_{\rm box}(i,T) - X_{\rm size},\ X_{\rm box}(i,T) + X_{\rm size}] \\ &\times [Z_{\rm box}(i,T) - Z_{\rm size},\ Z_{\rm box}(i,T) + Z_{\rm size}],\end{aligned} \tag{C4}$$

where $X_{\rm size}$ and $Z_{\rm size}$ are half the size of the ion box in the x and z directions. Then the rate of getting effective counts in the box of each ion is

$$\frac{dN_{\rm eff}(i,t)}{dt} = \begin{cases} dN_i(t)/dt & \text{if } (x(i,t), z(i,t)) \in \text{Range}(i,T) \\ 0 & \text{if } (x(i,t), z(i,t)) \notin \text{Range}(i,T). \end{cases}$$

Finally, the effective counts (the simulated photon counts in the main text) are calculated by

$$\text{Counts}(i,\ T) = \int_{T}^{T+\Delta T} \frac{dN_{\text{eff}}(i,t)}{dt} dt. \tag{C5}$$

Note that, to be compared with the actual photon counts in the experiment quantitatively, finite detection efficiency and the imperfection in the real imaging system have to be considered additionally.

APPENDIX D: ADDITIONAL EXPERIMENTAL DATA

In Figs. 6(a), 7, and 8, we show the experimental data for the results in Figs. 2, 3, and 4 of the main text, respectively.

[1] H. Mori, H. Okamoto, and S. Isa, A simplified theory of liquid-solid transitions. I, Prog. Theor. Phys. **47**, 1087 (1972).

[2] W. Paul, Electromagnetic traps for charged and neutral particles, Rev. Mod. Phys. **62**, 531 (1990).

[3] F. Penning, Die glimmentladung bei niedrigem druck zwischen koaxialen zylindern in einem axialen magnetfeld, Physica **3**, 873 (1936).

[4] H. Dehmelt, in *Advances in Atomic and Molecular Physics* Vol. 3 (Academic Press, New York, 1968), pp. 53–72.

[5] E. Wigner, On the interaction of electrons in metals, Phys. Rev. **46**, 1002 (1934).

[6] J. Sólyom, Wigner crystals: New realizations of an old idea, EPJ Web Conf. **78**, 01009 (2014).

[7] M. G. Raizen, J. M. Gilligan, J. C. Bergquist, W. M. Itano, and D. J. Wineland, Ionic crystals in a linear Paul trap, Phys. Rev. A **45**, 6493 (1992).

[8] T. B. Mitchell, J. J. Bollinger, D. H. E. Dubin, X.-P. Huang, W. M. Itano, and R. H. Baughman, Direct observations of structural phase transitions in planar crystallized ion plasmas, Science **282**, 1290 (1998).

[9] W. M. Itano, J. J. Bollinger, J. N. Tan, B. Jelenković, X.-P. Huang, and D. J. Wineland, Bragg diffraction from crystallized ion plasmas, Science **279**, 686 (1998).

[10] A. Mortensen, E. Nielsen, T. Matthey, and M. Drewsen, Observation of Three-Dimensional Long-Range Order in Small Ion Coulomb Crystals in an rf Trap, Phys. Rev. Lett. **96**, 103001 (2006).

[11] F. Diedrich, E. Peik, J. M. Chen, W. Quint, and H. Walther, Observation of a Phase Transition of Stored Laser-Cooled Ions, Phys. Rev. Lett. **59**, 2931 (1987).

[12] R. Blümel, J. Chen, E. Peik, W. Quint, W. Schleich, Y. Shen, and H. Walther, Phase transitions of stored laser-cooled ions, Nature **334**, 309 (1988).

[13] J. P. Schiffer, Order in confined ions, J. Phys. B: At. Mol. Opt. Phys. **36**, 511 (2003).

[14] M. Mazars, The melting of the classical two-dimensional Wigner crystal, Europhys. Lett. **110**, 26003 (2015).

[15] Q. A. Turchette, D. Kielpinski, B. E. King, D. Leibfried, D. M. Meekhof, C. J. Myatt, M. A. Rowe, C. A. Sackett, C. S. Wood, W. M. Itano *et al.*, Heating of trapped ions from the quantum ground state, Phys. Rev. A **61**, 063418 (2000).

[16] D. J. Wineland, C. Monroe, W. M. Itano, D. Leibfried, B. E. King, and D. M. Meekhof, Experimental issues in coherent quantum-state manipulation of trapped atomic ions, J. Res. Natl. Inst. Stand. Technol. **103**, 259 (1998).

[17] R. Blümel, C. Kappler, W. Quint, and H. Walther, Chaos and order of laser-cooled ions in a Paul trap, Phys. Rev. A **40**, 808 (1989).

[18] V. L. Ryjkov, X. Zhao, and H. A. Schuessler, Simulations of the rf heating rates in a linear quadrupole ion trap, Phys. Rev. A **71**, 033414 (2005).

[19] C. B. Zhang, D. Offenberg, B. Roth, M. A. Wilson, and S. Schiller, Molecular-dynamics simulations of cold single-species and multispecies ion ensembles in a linear Paul trap, Phys. Rev. A **76**, 012719 (2007).

[20] I. M. Buluta, M. Kitaoka, S. Georgescu, and S. Hasegawa, Investigation of planar Coulomb crystals for quantum simulation and computation, Phys. Rev. A **77**, 062320 (2008).

[21] V. T. Dolgopolov, Quantum melting of a two-dimensional Wigner crystal, Phys. Usp. **60**, 731 (2017).

[22] M. Ramm, T. Pruttivarasin, and H. Haeffner, Energy transport in trapped ion chains, New J. Phys. **16**, 063062 (2014).

[23] J. W. Emmert, M. Moore, and R. Blümel, Prediction of a deterministic melting transition of two-ion crystals in a Paul trap, Phys. Rev. A **48**, R1757 (1993).

[24] A. W. Vogt, Nonlinear resonances and the melting of Wigner crystals in a Paul trap, Phys. Rev. A **49**, R657 (1994).

[25] R. Blatt and D. Wineland, Entangled states of trapped atomic ions, Nature **453**, 1008 (2008).

[26] M. Drewsen, Ion Coulomb crystals, Physica B: Condens. Matter **460**, 105 (2015).

[27] J. I. Cirac and P. Zoller, Quantum Computations with Cold Trapped Ions, Phys. Rev. Lett. **74**, 4091 (1995).

[28] D. J. Berkeland, J. D. Miller, J. C. Bergquist, W. M. Itano, and D. J. Wineland, Laser-Cooled Mercury Ion Frequency Standard, Phys. Rev. Lett. **80**, 2089 (1998).

[29] S. Bharath, F. Martin, and L. Gerd, Measuring the temperature and heating rate of a single ion by imaging, New J. Phys. **21**, 113014 (2019).

[30] D. Leibfried, R. Blatt, C. Monroe, and D. Wineland, Quantum dynamics of single trapped ions, Rev. Mod. Phys. **75**, 281 (2003).

[31] J. Thijssen, *Computational Physics*, 2nd ed. (Cambridge University Press, Cambridge, UK, 2007).

[32] S. W. S. Apolinario and F. M. Peeters, Melting of anisotropically confined Coulomb balls, Phys. Rev. B **78**, 024202 (2008).

[33] F. Calvo, C. Champenois, and E. Yurtsever, Crystallization of ion clouds in octupole traps: Structural transitions, core melting, and scaling laws, Phys. Rev. A **80**, 063401 (2009).

[34] G.-D. Lin and L.-M. Duan, Equilibration and temperature distribution in a driven ion chain, New J. Phys. **13**, 075015 (2011).

[35] D. K. Weiss, Y. S. Nam, and R. Blümel, Lifetimes of metastable ion clouds in a Paul trap: Power-law scaling, Phys. Rev. A **93**, 043424 (2016).

[36] A. Pöschl, Master's thesis, Applied Physics. KTH, 2018.

[37] G. Vrijsen, Y. Aikyo, R. F. Spivey, I. V. Inlek, and J. Kim, Efficient isotope-selective pulsed laser ablation loading of $^{174}Yb^{+}$ ions in a surface electrode trap, Opt. Express **27**, 33907 (2019).

[38] A. Rosenfeld and J. L. Pfaltz, Sequential operations in digital picture processing, J. Assoc. Comput. Mach. **13**, 471 (1966).